





JGR Space Physics

RESEARCH ARTICLE

10.1029/2019JA027379

Electron Wing-Like Structures Formed at a Negatively Charged Spacecraft Moving in a Magnetized Plasma

Y. Miyake¹ , W. J. Miloch² , S. H. Kjus² , and H. L. Pécseli² 

¹Education Center on Computational Science and Engineering, Kobe University, Kobe, Japan, ²Department of Physics, University of Oslo, Oslo, Norway

Key Points:

- Electrons reflected at a negatively charged moving spacecraft form wing-like density structures in a magnetized plasma
- Electron wing-like structures are characterized by the trail of field-aligned propagation of Langmuir waves
- Reflected electrons cause spurious electric fields that can be measured by double probes on a satellite

Supporting Information:

- Supporting Information S1

Correspondence to:

Y. Miyake,
y-miyake@eagle.kobe-u.ac.jp

Citation:

Miyake, Y., Miloch, W. J., Kjus, S. H., & Pécseli, H. L. (2020). Electron wing-like structures formed at a negatively charged spacecraft moving in a magnetized plasma. *Journal of Geophysical Research: Space Physics*, 125, e2019JA027379. <https://doi.org/10.1029/2019JA027379>

Received 7 SEP 2019

Accepted 1 DEC 2019

Accepted article online 15 DEC 2019

Abstract Spacecraft-plasma interactions are studied with self-consistent numerical simulations of magnetized plasmas, where electrons are strongly magnetized whereas ions are weakly magnetized. It is found that for a spacecraft in such a magnetized plasma corresponding to a low Earth orbit, electrons can be reflected from a negatively charged spacecraft and then guided by geomagnetic field lines. The reflected electrons can leave a sharp trail like wings if the spacecraft size is greater than an average electron gyroradius of the environment. Such an electron wing-like structure is associated with propagating Langmuir waves. This results in nontrivial asymmetric electrostatic potentials close to the spacecraft and even farther than the Debye screening distance. The convective electric field also gives rise to a differential potential of the spacecraft with respect to the plasma, resulting in yet another asymmetry in the plasma dynamics and the potential distribution around the spacecraft. These asymmetries in the plasma dynamics can significantly influence in-situ measurements of space plasma. The results show a good qualitative agreement with actual measurements by a satellite in the polar regions.

1. Introduction

An object embedded in space plasmas will be electrically charged due to electron and ion currents to its surface. When the net current to the surface is zero, the object will be at floating potential with respect to the undisturbed surrounding plasma (Whipple, 1981; Garrett, 1981). Since electrons are much more mobile than ions, if only electron and ion currents are taken into account, the floating potential will be negative (Spitzer, 1941; Hastings, 1995). In cases where photoemission and secondary emission currents give a significant contribution to the net current, the floating potential can also reach positive values (Roussel & Berthelier, 2004; Engwall et al., 2006; Miloch & Vladimirov, 2009; Miloch et al., 2009; Yaroshenko et al., 2011).

The electric potential of a spacecraft will determine the dynamics of plasma particles in its vicinity. The charged spacecraft will disturb the plasma locally, giving rise to a sheath around it, where the plasma quasi-neutrality is locally broken (Robertson, 2013). Under stationary conditions (i.e., with no plasma flow around the spacecraft), the sheath usually extends to a few Debye lengths λ_D . Thus, to measure the undisturbed plasma, the instruments are often placed on booms far away from the main spacecraft body (Eriksson et al., 2006; Miyake et al., 2013; Spicher et al., 2016).

A spacecraft, such as satellite or rocket, is generally moving with respect to the plasma. In the low Earth orbits (LEO), the orbital speed is between 7 to 8 km/s. With the change in dominant ion species, the spacecraft can be supersonic at low altitudes, and subsonic at high altitudes. In both cases, a wake will form downstream of the spacecraft, which for supersonic flows can extend much farther than the Debye length from the spacecraft surface (Al'pert et al., 1966; Khrapak et al., 2005; Ludwig et al., 2012; Miloch, 2014; Darian et al., 2017; Paulsson et al., 2019).

The importance of the sheath and wake effects for in-situ measurements has been recognized early, and a number of studies were carried out to address this problem with increasingly more realistic models and simulations (Wang & Hastings, 1992; Scime et al., 1994; Torkar et al., 1998; Engwall et al., 2006; Svenes & Trøim, 1994; Garrett & Whittlesey, 2000; Anderson, 2012; Marchand et al., 2014; Miyake & Usui, 2016; Marchand & Lira, 2017; Capon et al., 2017). Due to the computational complexity, only recently, the effects of the magnetic field on the wake and spacecraft charging have been studied in self-consistent simulations (Marchand, 2012; Darian et al., 2017). In a magnetized plasma, which is found at LEO, the electron dynamics are controlled by the magnetic field, and thus, the wake can be modified as compared to the unmagnetized case,

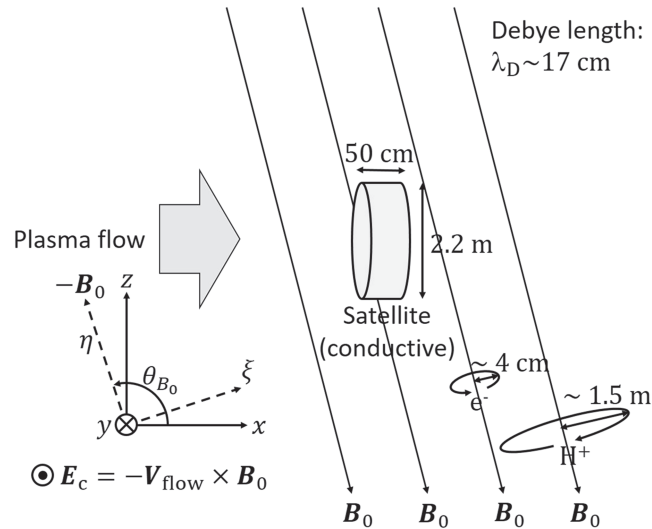


Figure 1. Simulation configuration considered in the present study.

and also become asymmetric (Darian et al., 2017; Usui et al., 2019). Note that an object in flowing plasmas is still one of outstanding problems of general interest in plasma physics, including complex plasmas, charging of solar system small bodies, or probe measurement techniques (Shukla & Mamun, 2002; Vladimirov et al., 2005; Holmström et al., 2012; Miyake & Nishino, 2015; Beadles et al., 2017; Darian et al., 2019).

Spin-stabilized spacecraft may probe the wake every spin period, which will contaminate the data and needs to be taken into account in the analysis (Scime et al., 1994; Paulsson et al., 2019). Taking the spin plane perpendicular to the flow might reduce this problem and improve data quality. However, in a magnetized plasma, the charged particle dynamics, and consequently the electric potential are often not axisymmetric in the plane perpendicular to the flow. One reason is the effect of the magnetic field on the electron dynamics. Another reason is the convective electric field originating from the $-\mathbf{V}_{\text{flow}} \times \mathbf{B}_0$ term (Pécsele, 2012), where \mathbf{V}_{flow} and \mathbf{B}_0 represent the vectors of the plasma flow and the Earth's magnetic field, respectively. The electric field is observed in the spacecraft frame of reference, and the onboard instruments will experience the potential change in the $\mathbf{V}_{\text{flow}} \times \mathbf{B}_0$ direction. This principle is actively utilized in the electrodynamic tether system (Cosmo & Lorenzini, 1997), whereas it is also known as a complicating factor for sounding rocket experiments, where the instruments are placed on extended booms (Sanmartin, 2010; Paulsson et al., 2019). While in the data analysis the convective electric field is usually easily removed, it is still an open question how the plasma, as seen from the spacecraft, will react to the effective potential of the spacecraft and how it will influence in-situ measurements.

In this work we investigate the dynamics of a magnetized plasma in the vicinity of a spacecraft, by means of three-dimensional particle-in-cell simulations. The code simulates a collisionless plasma as found at high altitudes in the Earth's near space environment. We consider a supersonic plasma flow and the magnetic field slightly tilted with respect to the satellite spin plane. Such a magnetic field will be relevant for satellites moving in the polar regions, but it also allows for studying a general problem with a magnetic field at a non-orthogonal angle with respect to the satellite orbit. We choose to simulate a plasma with parameters and conditions relevant for a spacecraft like the Freja satellite (Lundin et al., 1998). For the regions of interest here, the Freja satellite is spin stabilized with its spin vector in the direction of the movement (Eriksson et al., 1994; Pécsele et al., 1996; Høyemork et al., 2001). We have access to data from this satellite. In the present study, we demonstrate that both strong magnetization of electrons and convective electric fields significantly modify the plasma environment in the vicinity of the spacecraft.

2. Approach and Numerical Model

For numerical simulations, we employ an electrostatic version of the EMSES code, which is designed for the study of spacecraft-plasma interactions (Miyake & Usui, 2009). In the code, the coupled system of charged particle dynamics and electrostatic field evolution is solved in the standard particle-in-cell (PIC)

Table 1
Environmental and System Parameters in the Reference Simulation

Environmental parameters	
Plasma number density n_0	500 cm ⁻³
Electron temperature T_e	3,000 K
Ion composition	Hydrogen (100%)
Ion (H ⁺) temperature T_i	2,400 K
Debye length λ_D	17 cm
Average electron gyroradius r_{ge}	4 cm
Average ion gyroradius r_{gi}	1.5 m
Flow velocity V_{flow}	11 km/s
Geomagnetic field B_0	30 μ T
Magnetic field angle θ_{B_0} in the xz plane	95°
Electron plasma period τ_{pe}	5 μ s
Electron gyro period τ_{ge}	1.2 μ s
Ion plasma period τ_{pi}	0.21 ms
Ion gyro period τ_{gi}	2.2 ms
System parameters	
Grid width Δr	5 cm
Time step width Δt	0.025 μ s
Number of particles per cell	40 for each species
Domain size	25 ³ m ³
Physical time to be simulated	5 ms

method (Birdsall & Langdon, 1985; Hockney & Eastwood, 1981). That is, the motions of a bunch of charged macroparticles, each of which represents many real plasma particles, are advanced over small time steps, with a self-consistent electrostatic force field defined on computational grids. The updated particle distributions are mapped onto the grid space to obtain a new charge density profile. The density profile is used as a source term of Poisson's equation to calculate an updated electrostatic (or potential) field, and then the system equations are closed. To process this computational cycle, EMSES adopts a number of conventional techniques such as the Boris method for updating particle velocities (Boris, 1970; Birdsall & Langdon, 1985) and the spectral method for solving Poisson's equation (Hockney & Eastwood, 1981). Besides the electrostatic field, we can also consider a static magnetic field to push particles. More complete descriptions on EMSES are provided in previous works such as Miyake and Usui (2009) and Miyake and Usui (2016).

Figure 1 shows the simulation configuration. We consider a spacecraft body placed in an ionospheric plasma flow. The spacecraft is like a short cylinder, and its axis is aligned with the x axis of the simulation coordinates. The radius $r_{sc} = 2.2$ m and height $h_{sc} = 0.5$ m are determined by reference to the Freja satellite. The simulated plasma, composed of a large number of electrons and ions, is flowing in $+x$ direction. The major plasma parameters, listed in Table 1, are relevant for polar ionospheric conditions around 1,000–1,400 km altitude. With increasing altitude, the hydrogen ion H⁺ is the dominant species and is also considered in the simulations.

In the reference simulation, we employ the plasma flow velocity $V_{flow} = 1.65c_{ia} \sim 11$ km/s, where $c_{ia} = \sqrt{(k_B T_e + k_B T_i)/m_i} = 6.7$ km/s is the ion acoustic speed and k_B , m_i , T_e , and T_i are the Boltzmann constant, the ion mass, and the temperatures of electrons and ions, respectively. Such a supersonic regime is chosen to emphasize electrostatic perturbations caused by a moving spacecraft. Note that the simulations are carried out in the spacecraft frame of reference and V_{flow} represents the relative flow velocity between the spacecraft and the plasma. Since the value chosen for V_{flow} corresponds to approximately 1.5 times the typical orbital velocity (e.g., ~ 7.35 km/s at 1,000 km altitude) of the satellite, we also need to assume a rather fast convection of the plasma itself for such a flow condition. However, different velocities are also considered in the parametric study.

The uniform geomagnetic field $B_0 = 30 \mu\text{T}$ is applied to the whole simulation domain. For this field, an average gyroradius for electrons is smaller ($r_{ge} \sim 4 \text{ cm}$) than, and for ions is comparable ($r_{gi} \sim 1.5 \text{ m}$) to the spacecraft size. The field vectors are nearly in $-z$ direction, but with small inclination in the xz plane. Such a configuration simulates a satellite crossing the polar regions. We use the angle θ_{B_0} in the xz plane to define B_0 direction as shown in Figure 1. Since we consider a plasma flow across B_0 , we see a convection ($-\mathbf{V}_{\text{flow}} \times \mathbf{B}_0$) electric field in $-y$ direction throughout the simulation domain. Such an electric field is indeed measurable with instrumented satellites (Marklund et al., 1994).

Typical Alfvén wave velocities are of the order of 25 km/s at altitudes relevant for the plasma conditions discussed in this work (Kjus et al., 1998). Since spacecraft velocities are smaller than this Alfvén velocity, an electrostatic model should be adequate. A study by Rehman and Marchand (2014) considered magnetic perturbations generated in the vicinity of a spacecraft. The perturbations found in that work are very small, approximately 20 pT. They would have negligible consequences for our study.

A solid body of the spacecraft will absorb incoming electrons and ions and consequently get charged electrically. In this study, we do not consider photoelectron emission from the spacecraft. This treatment assumes that due to low solar zenith angle, the solar UV should be attenuated by the atmosphere, and the photoelectron yield is rather small. The spacecraft is assumed to have coating with conductive materials. Hence, an electric potential should be uniform over the surface. For this condition, satellite surface charges are kept redistributed throughout a simulation, based on the capacitance matrix method (Hockney & Eastwood, 1981).

The following treatments are employed for external boundaries and simulation duration. We remove outgoing particles from the domain, while at the same time, we keep supplying new particles with a prescribed flux, temperature, and drift velocity. We employ the Dirichlet condition for solutions of Poisson's equation, which means that a potential value is fixed at the boundaries. To obtain steady-state solutions, we run all simulations for durations longer than $10\tau_{pi}$, where $\tau_{pi} = 2\pi/\omega_{pi}$ represents the ion plasma period and ω_{pi} is the ion plasma frequency.

3. Simulation Results

3.1. Electrostatic Perturbations

Figure 2 shows the steady-state profiles of electron and ion densities, and electric potential obtained from the reference simulation with an ion-acoustic Mach number $M_{ia} = V_{\text{flow}}/c_{ia} = 1.65$. All the plots are in an xz plane that intersects with the spacecraft center, although the simulation itself is in three dimensions. Several features are already identified in this slice, although the plane is orthogonal to the convective electric field $\mathbf{E}_c = -\mathbf{V}_{\text{flow}} \times \mathbf{B}_0$ along the y axis. Behind the spacecraft, both electrons and ions are depleted as the spacecraft body blocks the plasma flow. The signature of clear wake formation is attributed to the supersonic regime of the flow, which prohibits ions from filling in a space immediately behind the spacecraft. The spacecraft body itself is charged to a negative value of $\phi_{sc} = -0.53 \text{ V}$, or $-2.1k_B T_e/e$, where e represents the elementary charge. It reflects that a thermal electron current dominates the spacecraft charging. The charged spacecraft exerts a repulsive force on electrons in its vicinity. This results in a thin electron-depleted layer (or an ion sheath) formed in the spacecraft front. The negative potential area is further extended downstream due to the absence of positive ions behind the spacecraft. Such electrostatic features are typical for solid obstacles placed in supersonic plasma flows even with static magnetic fields (Darian et al., 2017; Usui et al., 2019).

We also identify thin tubes of enhanced electron density, extending nearly in $\pm z$ (or in $\pm \eta$) directions from the spacecraft. This electron wing-like structure (referred to as just “wing” hereinafter) emanates from the electron-depleted sheath layer covering the spacecraft front surface. The wings are inclined with respect to the z axis, and the inclination is more pronounced for more oblique B_0 as presented in section 3.2. Although the result suggests the field-aligned nature of the structure, the wing direction actually deviates slightly even from the B_0 direction. A faint wing signature is also seen in the ion profile, while its actual location lies just downstream of the electron one. This displacement implies that electron tube extension is a leading phenomenon and is followed by an ion response. In correspondence to the electron and ion profiles, the electric potential also exhibits a wing structure with both negative and positive polarization bands. The outlined features of electrostatic perturbations are abstracted graphically in Figure 2d.

Similar wing structures emanating from moving obstacles, but seen in different field components and spatial scales, have been discussed extensively for Alfvén (Drell et al., 1965; Neubauer, 1980) and whistler (Stenzel &

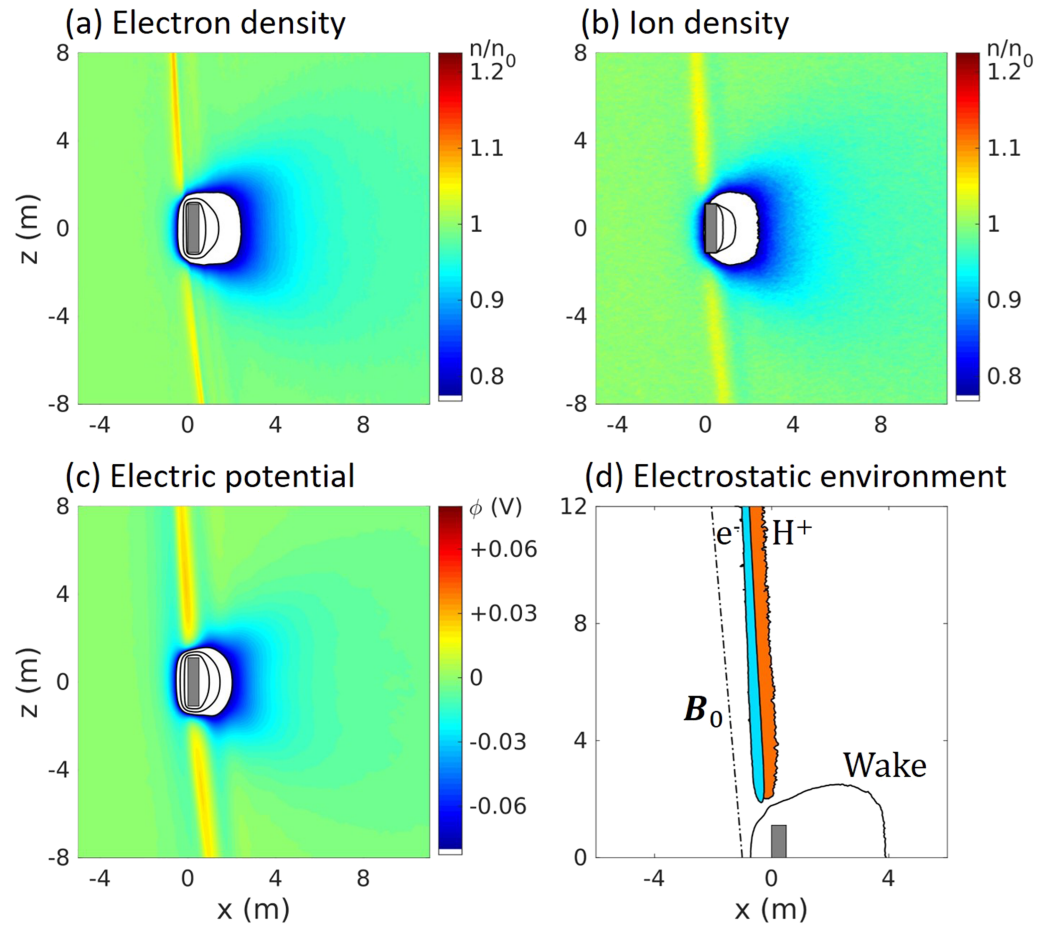


Figure 2. Two-dimensional (xz) slices of (a) electron density, (b) ion density, and (c) electric potential, obtained from the reference simulation. (d) The outlined electrostatic perturbations around the spacecraft.

Urrutia, 1989) waves. The main physical root of such wings are that some perturbations or waves extend out from obstacles with certain characteristic velocities, while being advected with the moving frame of plasma medium. The diverting angle thus contains information on what kind of wave mode is responsible for the wing formation. The angle is generally given as $\theta_w = \arctan(M^{-1})$, where θ_w is the wing angle measured from \mathbf{V}_{flow} and $M = V_{\text{flow}}/c$ denotes the Mach number with respect to the propagation speed c of the associated wave. If we take the ion-acoustic Mach number M_{ia} for the current problem, the angle will be too low to explain the results. In order to have the much higher angle of the identified wings, we need to take into account other wave modes associated with electron dynamics.

For identifying an associated wave, it is helpful to work on a simpler simulation configuration with $\mathbf{V}_{\text{flow}} \perp \mathbf{B}_0$, and a faster flow to emphasize the wing inclination. We additionally run a simulation with $\theta_{B_0} = 90^\circ$ and $M_{\text{ia}} = 3.3$, for which we expect larger wing inclination angle. The simulation result is displayed in Figure 3. Based on the vector diagram in the figure, the modified Mach angle relation is given by $|\theta_{B_0} - \theta_w| = \arctan(M) = \arctan(V_{\text{flow}}/c)$. Here, let us choose for c the Langmuir-mode group velocity for wavelengths λ comparable to or shorter than the Debye length, that is, $c_{L, \lambda \leq \lambda_D} \sim \sqrt{3k_B T_e / m_e} = 370$ km/s, where m_e represents the electron mass. (This is also the phase velocity in this short wavelength limit.) We then obtain an angle $|\theta_{B_0} - \theta_w| = \arctan(V_{\text{flow}}/c_{L, \lambda \leq \lambda_D}) = 3.4^\circ$. Based on the derived angle, we superpose the predicted wing trail with the dashed line, which appears to be in good agreement with the simulation result. Note that the above analysis provides only rough estimation, as the angle between the wing and \mathbf{B}_0 is rather small. In fact, the actual wing thickness along \mathbf{B}_0 is found to be greater than λ_D , as discussed in section 4. This means that the front speed c_L of Langmuir waves would be slower than 370 km/s, giving rise to a bit larger $|\theta_{B_0} - \theta_w| = \arctan(V_{\text{flow}}/c_L)$. Such small difference, however, is difficult to discern within the simulation domain employed herein.

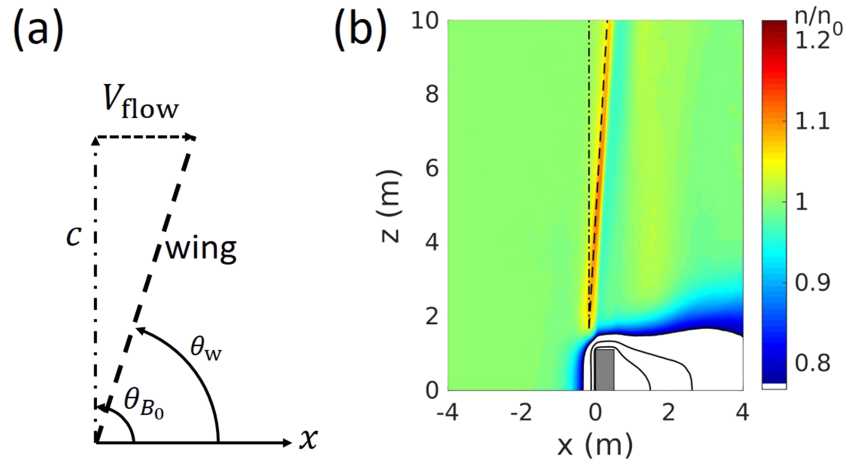


Figure 3. The associated wave analysis based on the wing direction, obtained from the simulation run with $\theta_{B_0} = 90^\circ$ and $M_{ia} = 3.3$. (a) Vector diagram (not scaled). (b) Electron density with the predicted wing trail (dashed line).

Based on the analysis, the electron wings (or “the Langmuir wings,” in analogy with the Alfvén wings) are produced in the following processes. Electrons approaching the spacecraft front are retarded and compressed by the negative potential of the spacecraft sheath, which leads to bump formation of electron density. The electron cluster is pushed away from the spacecraft position and guided to magnetic field lines due to substantial magnetization of electrons. The electron cluster then travels as propagating Langmuir waves in parallel to the field lines. Because the field line itself is also advected in the frame of reference considered herein, the series of processes leave a distinctive appearance like wings. Note that the phase at the wave

front (i.e., the electron wings) is almost constant, since the group and phase velocities are nearly the same in our case.

The proposed scenario can be confirmed in the simulations. Figure 4 displays the z component of an electron momentum flux obtained from the reference simulation. The plot clearly shows the presence of a field-aligned outflow of electrons inside the thin tubes corresponding to the wings. Although not displayed, we do not see such a field-aligned flow for ions, and thus, the ion enhancement behind the electron wings is the consequence of an ion-focusing (electrostatic lensing) effect caused by the excess of electron charges. Another interesting feature is an electron inflow to the spacecraft (i.e., a return current) found just behind the electron outflow. This signature is associated with electron loss at the spacecraft surface. This feature can be more pronounced in certain conditions, which will be demonstrated in section 3.3.

The identified wings are at angles much higher than the ion-acoustic Mach cone angle associated with the spacecraft wake. The wings, therefore, can interfere with double-probe measurements, even if the probes are deployed nearly perpendicular to the flow direction. This aspect will be studied in section 4.

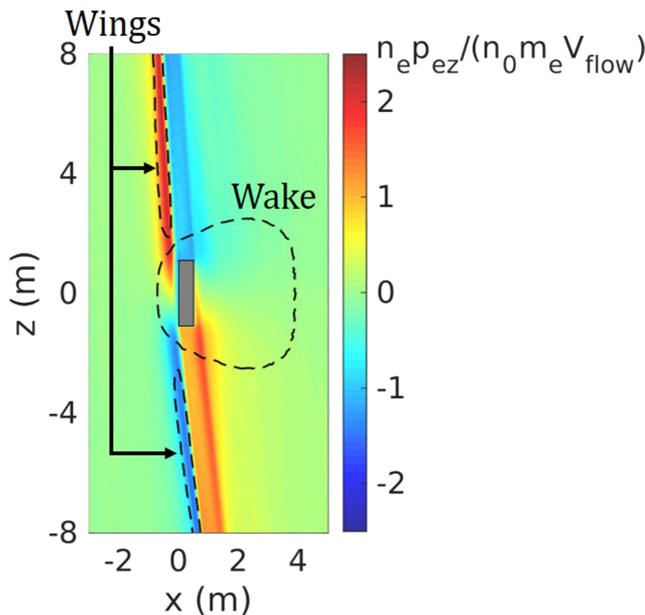


Figure 4. Two-dimensional (xz) slices of the z component of an electron momentum flux ($n_e p_{ez} / (n_0 m_e V_{\text{flow}})$) obtained from the reference simulation. The areas of the electron wings and the spacecraft wake, identified from the density plot, are indicated with dashed lines.

3.2. Dependence on Plasma Conditions

To study the parametric dependency of the identified structures, we performed additional simulations with different conditions in terms of the B_0 direction, flow velocity, and electron temperature. The resulting electron density profiles in xz plane are displayed in Figure 5. For each set of the parametric study, only a single parameter is altered, while other con-

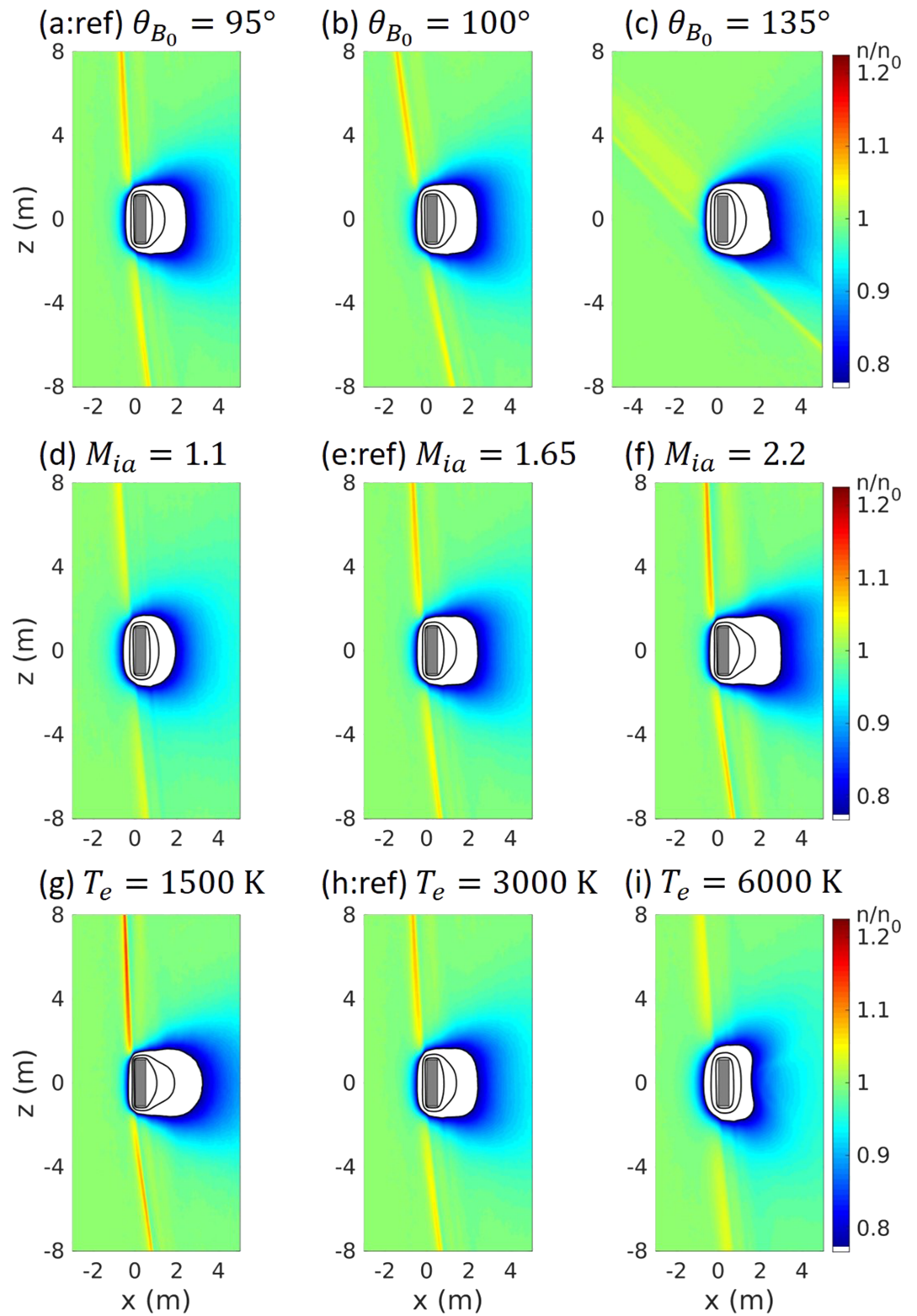


Figure 5. Parametric study of the electron wing signatures for various B_0 directions, flow velocities, and electron temperatures. Two-dimensional (xz) slices of electron density are shown.

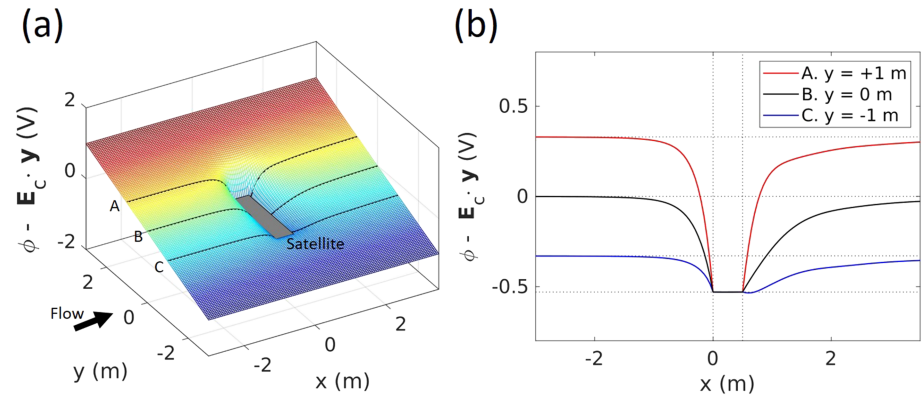


Figure 6. Electric potential structure with the $-\mathbf{V}_{\text{flow}} \times \mathbf{B}_0$ field. (a) Potential structure in the xy plane. The spacecraft position is displayed with the gray patch. (b) Potential profiles along the x axis on different y coordinates.

ditions remain unchanged. With varying \mathbf{B}_0 angle, the electron wings extend out at a different angle due to the field-aligned nature of the structure. It is interesting to note that the \mathbf{B}_0 direction also changes the electron density in the wings: that is, weaker wings for more oblique \mathbf{B}_0 .

The change in V_{flow} impacts the tilted angle of the electron wings according to the relation $|\theta_{\mathbf{B}_0} - \theta_w| = \arctan(V_{\text{flow}}/c_L)$. Higher V_{flow} also leads to further enhancement of electron density in the wings. The latter fact, that is, more intense wings for increasing V_{flow} , implies that a larger number of electrons are brought by a faster flow and are compressed at the ram face of the spacecraft. Such an effect depends also on the magnetic field angle with respect to the spacecraft ram face, and this aspect will be discussed in section 4. Note that the relative increase in the electron flux to the entire spacecraft is smaller than that of ions and thus the spacecraft potential becomes less negative for increasing V_{flow} . This is because the electron current (flowing along the η axis) is mostly collected on the lateral face of the spacecraft, and this current is unaffected by the change in V_{flow} .

The electron temperature should be another differentiating factor for the electron wing angle θ_w , as it will alter the group velocity of the Langmuir waves. This is confirmed in the parametric study here. An appreciable side effect would be its impact on the thickness of the electron tubes. The effect is regarded as a consequence of the altered degree of electron magnetization.

3.3. Effects of a Convective Electric Field

In the spacecraft frame of reference, we should observe a convective electric field \mathbf{E}_c . It follows immediately from $\nabla\phi = -\mathbf{E}_c = \mathbf{V}_{\text{flow}} \times \mathbf{B}_0$ that we will see a constant gradient in electric potential superposed anywhere in the simulated space, expect for within a spacecraft equipotential (conductive) body. This feature is visualized in Figure 6. The figure displays the potential structure on a xy plane, subject to be observed in the spacecraft frame of reference. The space potential has a gradient directed in $+y$, whereas the potential within the spacecraft body is constant. Note that, if we take a plasma frame of reference, the space potential should be constant and the potential within the conductive spacecraft should in turn have a gradient. What is important is, in either frame, a local spacecraft-to-plasma potential (i.e., an electric field intensity between them) will differ depending on the y coordinate.

The aforementioned effect leads to variable degrees of electron reflections that can be identified in different y coordinates. Figure 7 displays the electron density profiles on three xz slices rendered at A: $y = +1$, B: 0, and C: -1 m. The position of each slice is indicated in Figure 6, and the slice B corresponds to a midplane already plotted in Figure 2. In Slices A and B, there are substantial potential gaps between the spacecraft front and the plasma space. Thus, electron retardation and the resultant wing formation clearly take place. The electron bumps are a bit more pronounced in Slice A due to a greater potential gap. In contrast to these, electron bumps become less pronounced in Slice C. This is obviously attributed to a smaller potential gap. Electrons in this plane should experience a smaller repulsive force from the spacecraft.

Another remarkable feature seen in Slice C is the electron depletion that extend nearly along the magnetic field lines from the spacecraft body. This could be attributed to a rapid absorption of electrons by the spacecraft body, which in turn functions as a “plasma sink.” In fact, similar electron depletion takes place in other

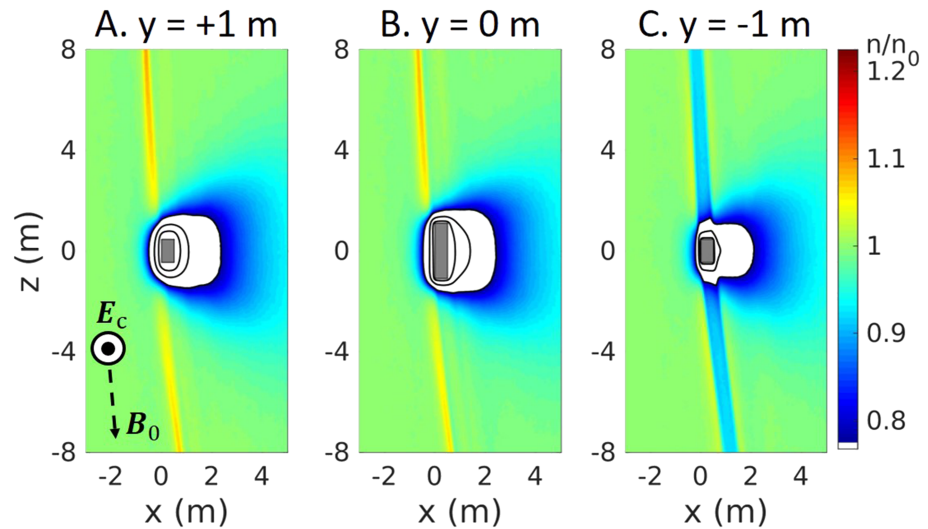


Figure 7. Two-dimensional (xz) profiles of electron density in planes with different y coordinates. Note that y position of each slice is also indicated in Figure 6.

slices, but to smaller degrees. This can be identified right downstream of the electron bump wings in Slices A and B. These electron dip wings become more prominent for smaller potential gaps, because the potential gap prohibits low-energy electrons from arriving and being captured at the spacecraft surface. The electron dips also propagate with a speed nearly consistent with propagating Langmuir waves.

The results outlined here demonstrate the effects of E_c that can change the features of the spacecraft-plasma interaction according to locations on the spacecraft. The pronounced contrast at different y coordinates is also attributed to substantial magnetization of electrons, which prevents exchange of electrons across different magnetic flux tubes.

4. Discussions

While electron reflections at the spacecraft sheath are important, they are not sufficient to explain the electron enhancement in the wings. Another requisite is a flow velocity to be faster than or at least in the same

order as the associated wave speed, which is in the present case $\sqrt{3k_B T_e/m_e} \sim 370$ km/s. It is often referred that we need at least ~ 0.3 Mach number to have appreciable fluid compression in the ram face of a moving obstacle (Anderson, 2016). The corresponding speed, however, is 110 km/s for the electron wave, and much higher than $V_{\text{flow}} \sim 11$ km/s employed in the present study.

In spite of the low values chosen for V_{flow} , the appreciable electron compression is possible thanks to strong magnetization of electrons. Provided that $r_{\text{ge}} \ll r_{\text{sc}}$, electrons in a certain flux tube will see a spacecraft front that approaches much faster than V_{flow} , because electron mobility is significant only along B_0 . This concept is graphically explained in Figure 8. For such a situation, it is helpful for an electron fluid to consider the de-Hoffmann-Teller transformation velocity $U_{\text{HT}} = (\tan \Delta\theta_{B_0})^{-1} V_{\text{flow}}$ (De Hoffmann & Teller, 1950), where $\Delta\theta_{B_0}$ denotes the angle between a certain magnetic field line and the obstacle surface. Given the plasma conditions, the condition $U_{\text{HT}} > 0.3\sqrt{3k_B T_e/m_e}$ will be met for $\Delta\theta_{B_0} < 5.7^\circ$. Thus, the present simulation configuration satisfies the condition required to have electron density enhancement within the wings.

In the discussion above, a negative potential surface (i.e., a potential wall), rather than the spacecraft surface, shall be regarded as an “obstacle,” and thus, the surface has an elliptic shape in the front of the spacecraft. It

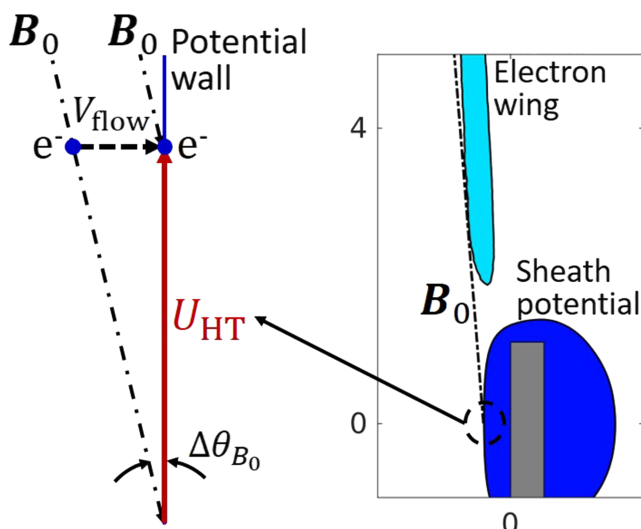


Figure 8. Schematics of the magnetic field line attaching the sheath potential wall. Electrons on this field line should see the potential wall, approaching with the speed U_{HT} in the de-Hoffmann-Teller frame, which is much faster than V_{flow} .

follows that all magnetic field lines attach the potential surface with $\Delta\theta_{B_0} \sim 0^\circ$. Consequently, an electron population experiences a potential wall approaching with $U_{HT} > \sqrt{3k_B T_e/m_e}$ at an initial stage of the attachment, resulting in effective electron compression and bump formation. The persistent time for such compression is strongly dependent on the sheath geometry as well as the magnetic field direction. With a higher U_{HT} , the density enhancement in the electron wings will be more prominent. This clearly explains the results of the parametric study presented in section 3.2, where the electron wing intensity was found to be dependent on both V_{flow} and θ_{B_0} .

It is also instructive to consider how far the electron wing can extend from the spacecraft position. The Langmuir waves with the wavelength $\lambda \leq \lambda_D$ will be strongly attenuated due to Landau damping. However, the wing has a Gaussian-like density structure in the direction parallel to \mathbf{B}_0 , as indicated in Figure 3b, and also in Figure S1 of the supporting information. Based on the supporting information, the full width at half maximum of the density bump is then identified to be within 2.3–3.1 m, as summarized in Table S1. This means that Langmuir wave components of wavelengths ranging from a few to several meters can be contained in the traveling wave. To estimate the electron wing distance, we use the damping rate γ_L of the Langmuir mode given as

$$\gamma_L = -\sqrt{\frac{\pi}{8}} \omega_{pe} \frac{(1 + 3k^2 \lambda_D^2)^2}{k^3 \lambda_D^3} \exp\left(-\frac{1}{2k^2 \lambda_D^2} - \frac{3}{2}\right), \quad (1)$$

where ω_{pe} and k denote the electron plasma frequency and the wave number, respectively. Assuming $k\lambda_D = 0.5$ and 0.25 (corresponding to wavelengths 2 and 4 m), we evaluate the period $T_{L,1/2}$, for which the wave amplitude will be attenuated to be the half, that is, $\exp(\gamma_L T_{L,1/2}) = 1/2$. With given parameters, it is calculated as $T_{L,1/2}/T_{pe} \sim 0.24$ and 31 for $k\lambda_D = 0.5$ and 0.25 , respectively. Hence, while shorter wavelength components will be damped rapidly, longer components can extend out tens of m, or hundreds of λ_D away from the spacecraft. This rough estimation suggests the presence of long-range electrostatic perturbations caused by the reflected electrons.

In closing, we consider implications of electron wing formation in the context of in-situ satellite observations. The Freja mission uses the standard double-probe technique for DC electric field measurements. An electric field is measured as a potential difference between two probes deployed by booms. The Freja satellite has three pairs of such double probes (six probes in total) deployed in its spin plane (Marklund et al., 1994). Despite its clear principle for measurement, the technique is often susceptible to electrostatic perturbations (Pedersen et al., 1998; Maynard, 1998). The Freja electric field experiments also identified such spurious effects, typically observed as electric field signals synchronized with a spin period, in the polar regions of the ionosphere. However, a spacecraft wake, which is often referred to as a source of spurious electric fields, is thought to be irrelevant for the double-probe measurements on the Freja satellite in the polar regions, as its spin plane is nearly perpendicular to the plasma flow direction. Thus, the electron wing formation could be the first to be suspected as a cause of such effects.

Figure 9a displays a few examples of electric field signals predicted by the numerical simulations. Note that we do not include the solid bodies of probes in the simulations. The plots are obtained by taking a potential difference between two positions on a circular orbit in the spin (i.e., yz) plane, at which probes are assumed to be placed. The orbit radius is $r_{dp} = 10$ m, and the electric field is calculated as $(\phi_{p1} - \phi_{p2})/2r_{dp}$, where ϕ_{p1} and ϕ_{p2} denote the local potentials at the assumed probe positions. The $-\mathbf{V}_{flow} \times \mathbf{B}_0$ component has been subtracted from the total field, and the shown signals are purely produced by the plasma-spacecraft interaction (i.e., spurious electric field).

Clear modulations are found in the signals around $\theta_{dp} = 90^\circ$ and 270° (the later is not shown), where θ_{dp} is the probe deployment angle with respect to the y axis. The modulations correspond to the timing for one of the probes crossing the electron wings, which nearly extend out to $\pm z$ directions. In correspondence to the electron bump and dip wings discussed earlier, the electric field also changes in both positive and negative polarization, and it occasionally shows a bipolar structure. The modulation amplitude and waveform are highly dependent on the plasma conditions. This feature is attributed to the thin (in the order of r_{ge}) structure of the wings. It should be noted that for $\theta_{B_0} = 90^\circ$, this kind of the electric field modulation should not take place, because the two opposite probes would experience the same potential modulation. Thus, a small inclination of \mathbf{B}_0 from the z axis is essential to explain the spurious effects.

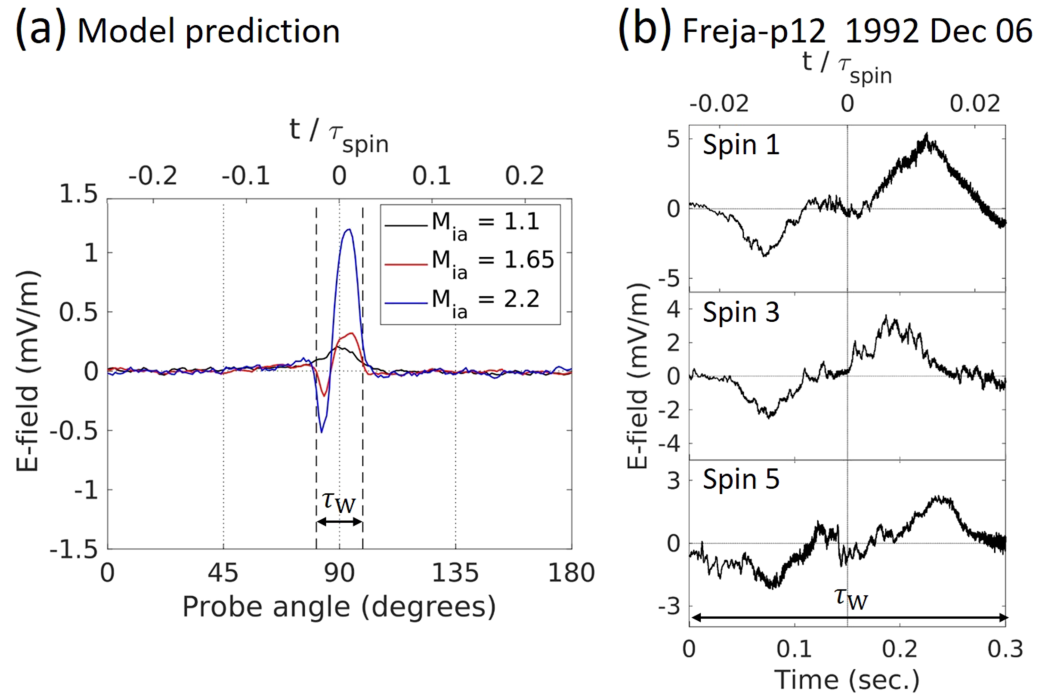


Figure 9. (a) Numerical prediction of electric field signals in the spacecraft-spin frame, subject to be measured by the double probes of 20 m tip-to-tip length. (b) Electric field waveforms observed by the Freja double-probe p12 during five spin periods starting at 02:12:25 on 6 December 1992. The selected waveforms are identified during the first, third, and fifth spin periods. Since the data are sampled within short bursts lasting 0.3–0.7 s, we show electric field signals within a time window of $\tau_W = 0.3$ s, the corresponding range in terms of a probe angle is displayed in panel (a). Note that the signals are shifted vertically by a constant from the raw data for better visibility. The common horizontal axis indicates the time t normalized to the satellite spin period $\tau_{\text{spin}} \sim 6.05$ s during this event.

In Figure 9b, we also display signals selected from the Freja in-situ observations in the polar regions. In order to have the solar panels facing the Sun in the region, the spin axis is nearly perpendicular to the local magnetic field of the Earth, as also assumed in the simulations. In correspondence to the numerical predictions, we have identified an isolated bipolar-like field modulation at a particular phase of each satellite spin. The pulse width of a few tenths of a second is consistent with the numerical predictions. A statistical study of in-situ observations also indicates that such electric field modulation was seen only for rather small angles of B_0 (typically, less than 15°) from the spin plane. The fact also supports the main conclusion rendered in the current numerical work. We should also note that the field amplitude is within the same order but somewhat greater in the observations. In addition to unavoidable uncertainties in actual plasma conditions, the exclusion of probe surfaces from the simulation model may contribute to this discrepancy. Further investigations on the current balance condition at the probe surface will elucidate the observed field amplitude caused by the electron wing formation.

5. Conclusions

We have numerically investigated electrostatic structures near the spacecraft moving in a magnetized plasma. In the environment corresponding to LEO, the spatial-scale range $r_{\text{ge}} \ll r_{\text{sc}} \sim r_{\text{gi}}$ normally holds among the electron/ion gyroradii and the spacecraft dimensions. The electrostatic particle-in-cell simulations have revealed that the substantial magnetization of electron causes a distinctive trail structure, which appears like wings. The wing structure is well characterized by Langmuir waves propagating along the magnetic field lines.

Depending on the spacecraft floating potential, both density bump (enhancement) and depletion can be found within the wings. In case without appreciable photoelectron emission as considered in the present study, the spacecraft floating potential is negative. The bump wings then become prominent due to electrons reflected and compressed by a repulsive sheath electric field. If the photoelectron emission current is taken

into account, although not simulated herein, the floating potential can be less negative, and the spacecraft in turn behaves more like a sink for approaching electrons. It will follow that the electron depletion wings are likely to be more pronounced. The auroral electrons, which are not considered either in the present study, are a possible factor making the floating potential more negative (Eriksson & Wahlund, 2006), and they will in turn strengthen the electron bump wings. These aspects will be interesting subjects to be investigated in the future work.

Interestingly, we have identified both bump and depletion wings in the present study, although we have not examined the photoemission effects. This is attributed to the convective electric field, which should be observed in the spacecraft frame of reference. Such a uniform field may be interpreted as a gradient in potential, whereas the potential should be constant over the conductive spacecraft surface. This means that the surface-to-plasma potential may differ according to location on the spacecraft surface. Attributed to this effect, we have captured a variety of electron wing features within one simulation run.

Numerical simulations can have particular value in distinguishing true plasma events from disturbances generated by moving rockets or satellites. This will be particularly important when studying nonequilibrium plasma conditions. In the examples presented here from the Freja satellite, we showed cases where the periodicity of the signals exactly coincided with the satellite spin. The present simulation results strongly suggested that the observed signals were spacecraft generated and not naturally occurring plasma waves.

The present study suggests a spurious factor of the third kind for probe measurements in the LEO environment, in addition to well-known sheath and wake effects. Its striking features are summarized as follows: (1) electrostatic perturbations developed nearly along the magnetic field lines, (2) perturbations like high-directivity electron beams, and (3) long-range perturbations extending much farther than Debye screening distances. In recognition of these features, the probe measurement contamination caused by the electron wings should be distinguished from the other types of spurious effects caused by spacecraft sheaths and wakes. Owing to their long-range nature, the contamination caused by the wings will be more difficult to avoid by separating the probes from the spacecraft. However, with sufficient attention in observation data analysis, such contaminated signals will be identifiable, as the wing will only affect a limited fraction of a rotating-probe orbit.

Acknowledgments

The research is the result of the Japan-Norway Partnership on Space Science Simulations, funded by the Norwegian Agency for International Cooperation and Quality Enhancement in Higher Education, Diku, Grant 212005 UTF-2016-long-term/10054, and is a part of the 4DSpace Strategic Research Initiative at the University of Oslo. The technical assistance by Bjørn Lybekk is gratefully acknowledged. The present study was also supported in part by the Japan Society for the Promotion of Science: JSPS (Grant 17K14403), the innovative High-Performance Computing Infrastructure: HPCI (Project HP190132), and the Joint Usage/Research Center for Interdisciplinary Large-scale Information Infrastructures: JHPCN (Project JH180018) in Japan. The computations in the present study were performed using the KDK system at the Research Institute for Sustainable Humanosphere (RISH), Kyoto University, the supercomputer system at the Information Initiative Center, Hokkaido University, and the Fujitsu FX100 Supercomputer at the Information Technology Center, Nagoya University, Japan. All data presented here can be retrieved from the Zenodo open-access repository (at <https://doi.org/10.5281/zenodo.3534594>).

References

- Al'pert, Y. L., Gurevich, A. V., & Pitaevskii, L. P. (1966). Space physics with artificial satellites. *American Journal of Physics*, *34*(6), 544–544. <https://doi.org/10.1119/1.1973101>
- Anderson, J. D. Jr. (2016). *Fundamentals of aerodynamics* (p. 1152). New York, NY: McGraw-Hill Inc.
- Anderson, P. C. (2012). Characteristics of spacecraft charging in low Earth orbit. *Journal of Geophysical Research*, *117*, A07308. <https://doi.org/10.1029/2011ja016875>
- Beadles, R., Wang, X., & Horányi, M. (2017). Floating potential measurements in plasmas: From dust to spacecraft. *Physics of Plasmas*, *24*(2), 023701. <https://doi.org/10.1063/1.4975610>
- Birdsall, C. K., & Langdon, A. B. (1985). *Plasma physics via computer*, (p. 512). New York, NY: McGraw-Hill Inc.
- Boris, J. P. (1970). Relativistic plasma simulation—optimization of a hybrid code. Proc. In *4th Conf. Num. Sim. Plasmas*, (pp. 3–67). Washington, DC: the Naval Research Laboratory.
- Capon, C. J., Brown, M., & Boyce, R. R. (2017). Scaling of plasma–body interactions in low Earth orbit. *Physics of Plasmas*, *24*(4), 042901. <https://doi.org/10.1063/1.4979191>
- Cosmo, M. L., & E. C. Lorenzini (1997). Tethers in space handbook, 234 pp., Smithsonian Astrophysical Observatory.
- Darian, D., Marholm, S., Paulsson, J. J. P., Miyake, Y., Usui, H., Mortensen, M., & Miloch, W. J. (2017). Numerical simulations of a sounding rocket in ionospheric plasma: Effects of magnetic field on the wake formation and rocket potential. *Journal of Geophysical Research: Space Physics*, *122*, 9603–9621. <https://doi.org/10.1002/2017ja024284>
- Darian, D., Miloch, W. J., Mortensen, M., Miyake, Y., & Usui, H. (2019). Numerical simulations of a dust grain in a flowing magnetized plasma. *Physics of Plasmas*, *26*(4), 043701. <https://doi.org/10.1063/1.5089631>
- De Hoffmann, F., & Teller, E. (1950). Magneto-hydrodynamic shocks. *Physical Review*, *80*(4), 692–703. <https://doi.org/10.1103/PhysRev.80.692>
- Drell, S. D., Foley, H. M., & Ruderman, M. A. (1965). Drag and propulsion of large satellites in the ionosphere An Alfvén propulsion engine in space. *Journal of Geophysical Research (1896-1977)*, *70*(13), 3131–3145. <https://doi.org/10.1029/JZ070i013p03131>
- Engwall, E., Eriksson, A. I., & Forest, J. (2006). Wake formation behind positively charged spacecraft in flowing tenuous plasmas. *Physics of Plasmas*, *13*(6), 062904. <https://doi.org/10.1063/1.2199207>
- Eriksson, A. I., André, M., Klecker, B., Laakso, H., Lindqvist, P.-A., Mozer, F., et al. (2006). Electric field measurements on Cluster: Comparing the double-probe and electron drift techniques. *Annales de Geophysique*, *24*(1), 275–289. <https://doi.org/10.5194/angeo-24-275-2006>
- Eriksson, A. I., Holback, B., Dovner, P. O., Boström, R., Holmgren, G., André, M., et al. (1994). Freja observations of correlated small-scale density depletions and enhanced lower hybrid waves. *Geophysical Research Letters*, *21*(17), 1843–1846. <https://doi.org/10.1029/94GL00174>

- Eriksson, A. I., & Wahlund, J. (2006). Charging of the Freja satellite in the Auroral zone. *IEEE Transactions on Plasma Science*, 34(5), 2038–2045. <https://doi.org/10.1109/TPS.2006.883373>
- Garrett, H. B. (1981). The charging of spacecraft surfaces. *Reviews of Geophysics*, 19(4), 577–616. <https://doi.org/10.1029/RG019i004p00577>
- Garrett, H. B., & Whittlesey, A. C. (2000). Spacecraft charging, an update. *IEEE Transactions on Plasma Science*, 28(6), 2017–2028. <https://doi.org/10.1109/27.902229>
- Hastings, D. E. (1995). A review of plasma interactions with spacecraft in low Earth orbit. *Journal of Geophysical Research/Physics*, 100, 14,457–14,483. <https://doi.org/10.1029/94JA03358>
- Hockney, R. W., & Eastwood, J. W. (1981). *Computer simulation using particles*, (p. 564). Oxford, UK: Taylor & Francis Inc.
- Holmström, M., Fatemi, S., Futaana, Y., & Nilsson, H. (2012). The interaction between the Moon and the solar wind, Earth. *Planets and Space*, 64(2), 17. <https://doi.org/10.5047/eps.2011.06.040>
- Hoymork, S. H., Pécseli, H. L., Lybekk, B., Trulsen, J., & Eriksson, A. (2001). The shape and evolution of lower hybrid density cavities observed by FREJA, Physics and Chemistry of the Earth, Part C: Solar. *Terrestrial & Planetary Science*, 26(1), 213–217. [https://doi.org/10.1016/S1464-1917\(00\)00110-0](https://doi.org/10.1016/S1464-1917(00)00110-0)
- Khrapak, S. A., Ivlev, A. V., Zhdanov, S. K., & Morfill, G. E. (2005). Hybrid approach to the ion drag force. *Physics of Plasmas*, 12(4), 042308. <https://doi.org/10.1063/1.1867995>
- Kjus, S. H., Pécseli, H. L., Lybekk, B., Holtet, J., Trulsen, J., Lühr, H., & Eriksson, A. (1998). Statistics of the lower hybrid wave cavities detected by the Freja satellite. *Journal of Geophysical Research*, 103(A11), 26,633–26,647. <https://doi.org/10.1029/98JA02245>
- Ludwig, P., Miloch, W. J., Kählert, H., & Bonitz, M. (2012). On the wake structure in streaming complex plasmas. *New Journal of Physics*, 14(5), 053016. <https://doi.org/10.1088/1367-2630/14/5/053016>
- Lundin, R., Haerendel, G., & Grahn, S. (1998). Introduction to special section: The Freja Mission. *Journal of Geophysical Research*, 103(A3), 4119–4123. <https://doi.org/10.1029/98JA00322>
- Marchand, R. (2012). PTetra, a tool to simulate low orbit satellite–plasma interaction. *IEEE Transactions on Plasma Science*, 40(2), 217–229. <https://doi.org/10.1109/TPS.2011.2172638>
- Marchand, R., & Lira, P. A. R. (2017). Kinetic simulation of spacecraft–environment interaction. *IEEE Transactions on Plasma Science*, 45(4), 535–554. <https://doi.org/10.1109/TPS.2017.2682229>
- Marchand, R., Miyake, Y., Usui, H., Deca, J., Lapenta, G., Matéo-Vélez, J. C., et al. (2014). Cross-comparison of spacecraft–environment interaction model predictions applied to Solar Probe Plus near perihelion. *Physics of Plasmas*, 21(6), 062901. <https://doi.org/10.1063/1.4882439>
- Marklund, G. T., Blomberg, L. G., Lindqvist, P.-A., Fälthammar, C. G., Haerendel, G., Mozer, F. S., et al. (1994). The double probe electric field experiment on Freja: Experiment description and first results. *Space Science Reviews*, 70(3), 483–508. <https://doi.org/10.1007/bf00756883>
- Maynard, N. C. (1998). Electric field measurements in moderate to high density space plasmas with passive double probes, pp. 13–27. <https://doi.org/10.1002/9781118664391.ch2>
- Miloch, W. J. (2014). Numerical simulations of dust charging and wakefield effects. *Journal of Plasma Physics*, 80(6), 795–801. <https://doi.org/10.1017/S0022377814000300>
- Miloch, W. J., & Vladimirov, S. V. (2009). Charging of spinning insulating objects by plasma and photoemission. *Geophysical Research Letters*, 36, L18110. <https://doi.org/10.1029/2009gl040337>
- Miloch, W. J., Vladimirov, S. V., Pécseli, H. L., & Trulsen, J. (2009). Charging of insulating and conducting dust grains by flowing plasma and photoemission. *New Journal of Physics*, 11(4), 043005. <https://doi.org/10.1088/1367-2630/11/4/043005>
- Miyake, Y., Cully, C. M., Usui, H., & Nakashima, H. (2013). Plasma particle simulations of wake formation behind a spacecraft with thin wire booms. *Journal of Geophysical Research: Space Physics*, 118, 5681–5694. <https://doi.org/10.1002/jgra.50543>
- Miyake, Y., & Nishino, M. N. (2015). Electrostatic environment near lunar vertical hole: 3D plasma particle simulations. *Icarus*, 260, 301–307. <https://doi.org/10.1016/j.icarus.2015.07.011>
- Miyake, Y., & Usui, H. (2009). New electromagnetic particle simulation code for the analysis of spacecraft–plasma interactions. *Physics of Plasmas*, 16(6), 062904. <https://doi.org/10.1063/1.3147922>
- Miyake, Y., & Usui, H. (2016). Particle-in-cell modeling of spacecraft–plasma interaction effects on double-probe electric field measurements. *Radio Science*, 51(12), 1905–1922. <https://doi.org/10.1002/2016rs006095>
- Neubauer, F. M. (1980). Nonlinear standing Alfvén wave current system at Io: Theory. *Journal of Geophysical Research*, 85(A3), 1171–1178. <https://doi.org/10.1029/JA085iA03p01171>
- Paulsson, J. J. P., Miyake, Y., Miloch, W. J., & Usui, H. (2019). Effects of booms of sounding rockets in flowing plasmas. *Physics of Plasmas*, 26(3), 032902. <https://doi.org/10.1063/1.5051414>
- Pécseli, H. L. (2012). *Waves and oscillations in plasmas*, (p. 575). Boca Raton, FL: CRC Press.
- Pécseli, H. L., Iranpour, K., Holter, Ø., Lybekk, B., Holtet, J., Trulsen, J., et al. (1996). Lower hybrid wave cavities detected by the FREJA satellite. *Journal of Geophysical Research*, 101(A3), 5299–5316. <https://doi.org/10.1029/95ja03127>
- Pedersen, A., F. Mozer, & G. Gustafsson (1998). Electric field measurements in a tenuous plasma with spherical double probes, pp. 1–12. <https://doi.org/10.1002/9781118664391.ch1>
- Robertson, S. (2013). Sheaths in laboratory and space plasmas. *Plasma Physics and Controlled Fusion*, 55(9), 093001. <https://doi.org/10.1088/0741-3335/55/9/093001>
- Roussel, J.-F., & Berthelier, J.-J. (2004). A study of the electrical charging of the Rosetta orbiter: 1 Numerical model. *Journal of Geophysical Research*, 109, A01104. <https://doi.org/10.1029/2003ja009836>
- Rehman, S., & Marchand, R. (2014). Plasma-satellite interaction driven magnetic field perturbations. *Physics of Plasmas*, 21(9), 090701. <https://doi.org/10.1063/1.4894678>
- Sanmartin, J. R. (2010). A review of electrodynamic tethers for science applications. *Plasma Sources Science and Technology*, 19(3), 034,022. <https://doi.org/10.1088/0963-0521/19/3/034022>
- Scime, E. E., Phillips, J. L., & Bame, S. J. (1994). Effects of spacecraft potential on three-dimensional electron measurements in the solar wind. *Journal of Geophysical Research*, 99(A8), 14,769–14,776. <https://doi.org/10.1029/94ja00489>
- Shukla, P. K., & Mamun, A. A. (2002). *Introduction to dusty plasma physics*, *Plasma Physics*, (p. 284). Boca Raton, FL: CRC Press. <https://doi.org/10.1088/0741-3335/44/3/701>
- Spicher, A., Ilyasov, A. A., Miloch, W. J., Chernyshov, A. A., Clausen, L. B. N., Moen, J. I., et al. (2016). Reverse flow events and small-scale effects in the cusp ionosphere. *Journal of Geophysical Research: Space Physics*, 121, 10,466–10,480. <https://doi.org/10.1002/2016JA022999>
- Spitzer, L. J. (1941). The dynamics of the interstellar medium. I. Local Equilibrium, vol. 93, 369 pp. <https://doi.org/10.1086/144273>
- Stenzel, R. L., & Urrutia, J. M. (1989). Whistler wings from moving electrodes in a magnetized laboratory plasma. *Geophysical Research Letters*, 16(5), 361–364. <https://doi.org/10.1029/GL016i005p00361>

- Svenes, K. R., & Trøim, J. (1994). Laboratory simulation of vehicle–plasma interaction in low Earth orbit. *Planetary and Space Science*, 42(1), 81–94. [https://doi.org/10.1016/0032-0633\(94\)90144-9](https://doi.org/10.1016/0032-0633(94)90144-9)
- Torkar, K., Veselov, M. V., Afonin, V. V., Arends, H., Fehringer, M., Fremuth, G., et al. (1998). An experiment to study and control the Langmuir sheath around INTERBALL-2. *Annales Geophysicae*, 16(9), 1086–1096. <https://doi.org/10.1007/s00585-998-1086-6>
- Usui, H., Miyake, Y., Miloch, W. J., & Ito, K. (2019). Numerical study of plasma depletion region in a satellite wake. *IEEE Transactions on Plasma Science*, 1–7. <https://doi.org/10.1109/TPS.2019.2918789>
- Vladimirov, S. V., Ostrikov, K., & Samarian, A. A. (2005). Physics and applications of complex plasmas. *Physics and Applications of Complex Plasmas*, 456. <https://doi.org/10.1142/p397>
- Wang, J., & Hastings, D. E. (1992). Ionospheric plasma flow over large high-voltage space platforms II: The formation and structure of plasma wake. *Physics of Fluids B: Plasma Physics*, 4(6), 1615–1629. <https://doi.org/10.1063/1.860070>
- Whipple, E. C. (1981). Potentials of surfaces in space. *Reports on Progress in Physics*, 44(11), 1197–1250. <https://doi.org/10.1088/0034-4885/44/11/002>
- Yaroshenko, V. V., Miloch, W. J., Vladimirov, S., Thomas, H. M., & Morfill, G. E. (2011). Modeling of Cassini's charging at Saturn orbit insertion flyby. *Journal of Geophysical Research*, 116, A12218. <https://doi.org/10.1029/2011ja016775>